We are IntechOpen,
the world's leading publisher of
Open Access books
Built by scientists, for scientists

6,900
Open access books available

185,000
International authors and editors

200M
Downloads

154
Countries delivered to

Our authors are among the

TOP 1%
most cited scientists

12.2%
Contributors from top 500 universities

CLARIVATE ANALYTICS
BOOK CITATION INDEX
INDEXED

WEB OF SCIENCE™

Selection of our books indexed in the Book Citation Index
in Web of Science™ Core Collection (BKCI)

Interested in publishing with us?
Contact book.department@intechopen.com

Chapter

Enhanced Humidity Sensing Response in Eu^{3+}-Doped Iron-Rich CuFe$_2$O$_4$: A Detailed Study of Structural, Microstructural, Sensing, and Dielectric Properties

I.C. Sathisha, K. Manjunatha, V. Jagadeesha Angadi,
B. Chethan, Y.T. Ravikiran, Vinayaka K. Pattar,
S.O. Manjunatha and Shidaling Matteppanavar

Abstract

The CuFe$_{(2-x)}$Eu$_x$O$_4$ (where x = 0.00, 0.01, 0.02, 0.03) nanoparticles are synthesized by solution combustion method. The influence of Eu^{3+} on the structural, morphological, dielectrical, and humidity sensing study is recorded. The XRD pattern peaks of the as-prepared CuFe$_{(2-x)}$Eu$_x$O$_4$ (where x = 0.00, 0.01, 0.02, 0.03) nanoparticle confirm the polycrystalline spinel cubic structure with a small amount of CuO impurity phase at 38.87° and 48.96°. Surface morphology of the samples was studied by scanning electron microscope (SEM) images of the nanoparticles, and their respective average grain size was estimated using Image software. Chemical composition of all prepared samples was analyzed by EDS spectra. The dielectric parameters of AC conductivity, electric modulus, and impedance of the samples were measured over a range of frequencies from 0.1 KHz to 1 MHz at room temperature. Europium-doped copper ferrite samples showed good humidity sensing response, response and recover times, and stability over a %RH range of 11–91%. These types of samples are very useful for sensor application, battery applications, electronic applications, and automotive applications.

Keywords: ferrite, Eu-doping, dielectric, impedance, humidity sensing

1. Introduction

In recent years, the great developments in the applications of larger ionic rare earth-doped ferrites have been effectively realized in many prominent fields mainly in sensors, communication, and electronics. Copper ferrite metal oxide is a *p*-type semiconductor metal oxide and has been used in organic synthesis as a catalyst. Recently, many research groups have explored the importance of copper ferrite metal oxide in wide advanced applications because of their unique chemical, biocompatible, and physical properties [1]. The CuFe$_2$O$_4$ ferrite has spinel cubic

structure with general formula Fd3m. The $CuFe_2O_4$ ferrite belongs to a general formula AB_2O_4 in which A is a divalent ion site occupied by the Cu^{2+} ions and B is a trivalent ion site occupied by Fe^{3+} ions. The rare earth-doped $CuFe_2O_4$ ferrites have been used in many fields such as electronic devices, drug delivery systems, cancer therapy, and magnetic recording [1]. Rare earth-doped ferrites are also useful in high voltage electronics due to its negligible eddy current losses, high electrical resistivity, high permeability, magneto-optical, and magnetoresistive properties [2–4]. Generally, the trivalent ions are lesser in size than a divalent ion, and hence exchange of cations among the A and B sites plays a vital role in studying the structural, morphological, dielectric, and humidity sensing behavior of spinel copper ferrites. Copper ferrite has considerable good attraction of potential applications in various devices, like cores in transformers and microwave absorption [3, 4]. Copper ferrite nanoparticles can be prepared by various techniques like sol-gel method, coprecipitation method, solution combustion method, etc. [5, 6]. Many researchers have explored the properties of spinel ferrites by doping with different larger rare earth ions like samarium, terbium, gadolinium, and cerium in it. The europium-doped copper ferrites can be used in high-frequency applications due to the rare earth-doped ferrites showing low dielectric loss, good sensing response, and low value of conductivity. Europium-doped copper ferrites are usually considered as inverse spinel ferrites.

In the present work, spinel copper ferrites were prepared by solution combustion method and then in Eu^{3+} ions will be incorporated to investigate its structural, morphological, dielectric, and humidity sensing behavior at room temperature.

2. Experimental details

2.1 Required oxidizers and fuels

The required oxidizers (metal nitrates), viz., copper nitrate [$Cu(NO_3)_2 \cdot 3H_2O$], europium nitrate [$Eu(NO_3)_3 \cdot 5H_2O$], and ferric nitrate [$Fe(NO_3)_2 \cdot 9H_2O$], and reducing agents, viz., carbamide [NH_2CONH_2] and glucose [$C_6H_{12}O_6$], all were purchased from S.D. Fine Chemicals, Mumbai, India.

2.2 Method

The $CuFe_{(2-x)}Eu_xO_4$ (where x = 0.00, 0.01, 0.02, 0.03) nanoparticles were synthesized by solution combustion method by using stoichiometry amount of copper nitrate, europium nitrate, and ferric nitrate as metal nitrates and carbamide and glucose as fuels. The weighed metal nitrates and fuels were taken in 250 ml borosil glass beaker; then all nitrates and fuels were diluted with distilled water and kept on magnetic stirrer about 45 min to obtain a homogeneous solution. This solution was kept in preheated muffle furnace at $450 \pm 10°C$ temperature to ignite, to get a copper ferrite nanoparticle. Obtained $CuFe_{(2-x)}Eu_xO_4$ (where x = 0.00, 0.01, 0.02, 0.03) nanoparticles were taken in to mortar and then pestle it for getting fine powder of nanoparticles. The solution combustion technique flowchart for europium-doped copper ferrite as shown in **Figure 1**.

2.3 Characterizations

For as-synthesized $CuFe_{(2-x)}Eu_xO_4$ (where x = 0.00, 0.01, 0.02, 0.03) nanoparticles, X-ray diffraction characterization was carried out by using
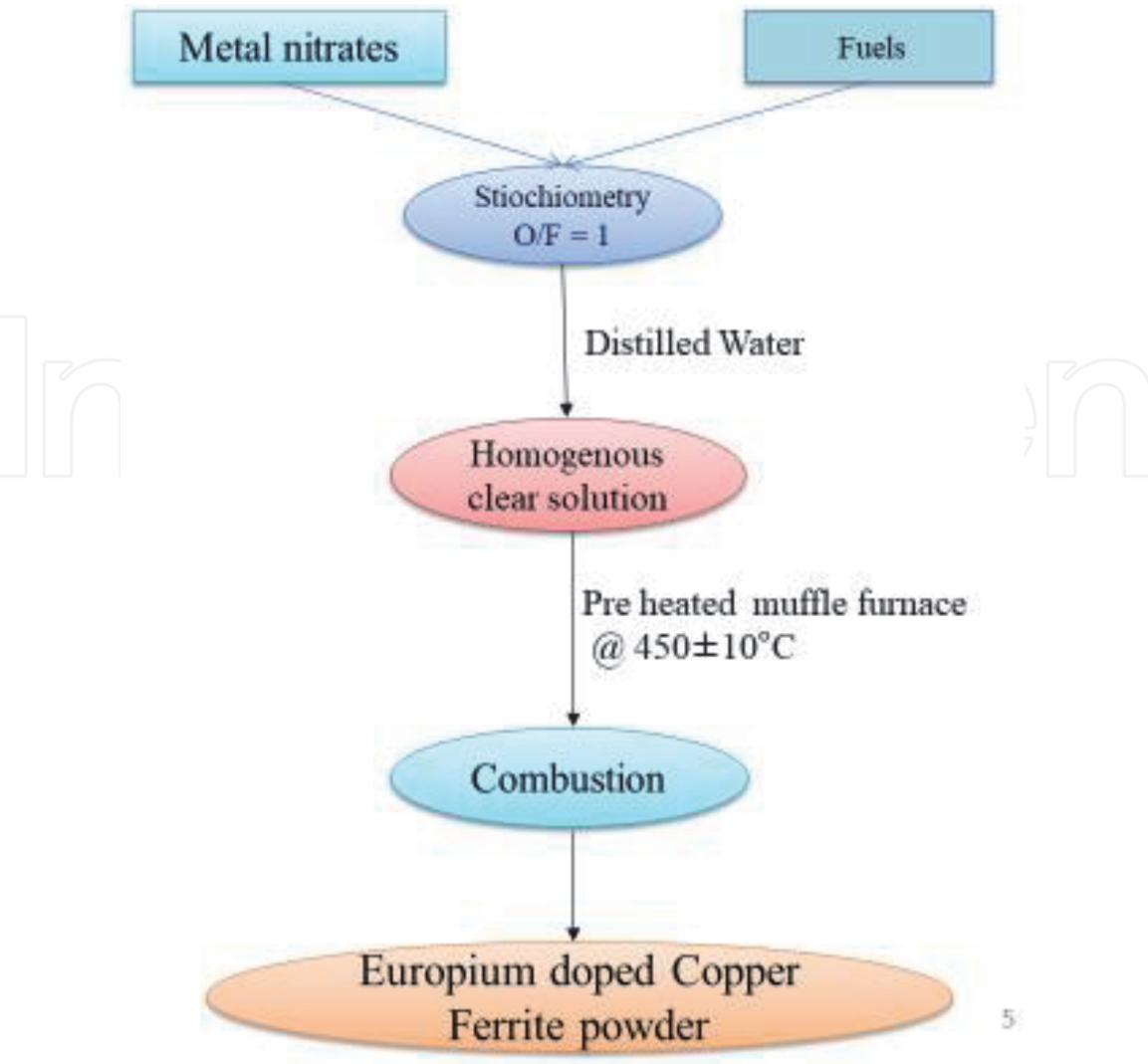
Figure 1.
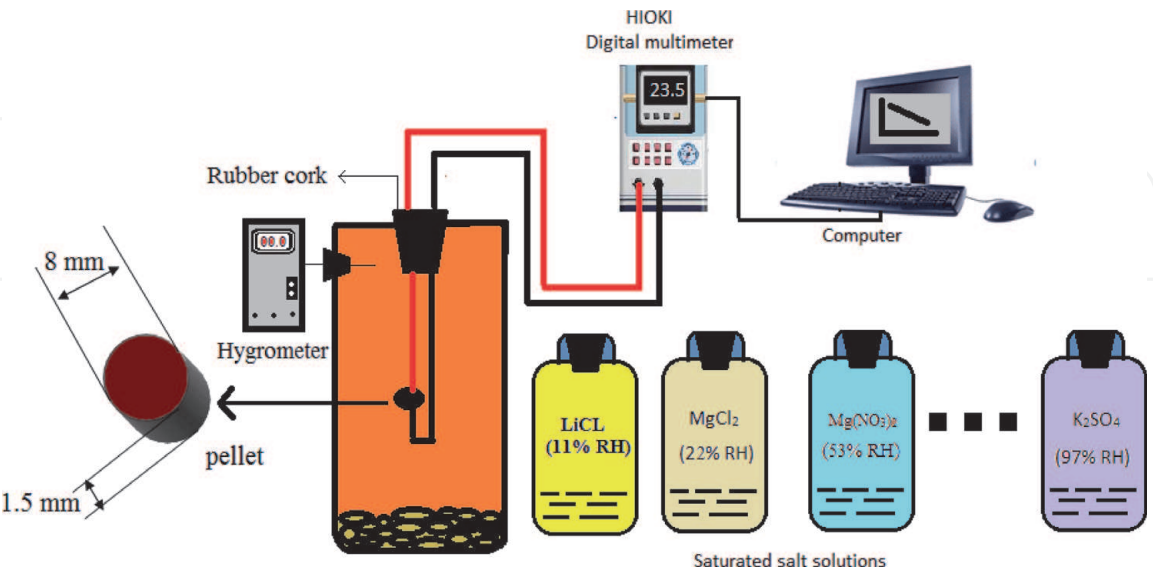*Flowchart to show solution combustion technique of synthesizing europium-doped copper ferrite.*

Figure 2.
Schematic illustration of humidity sensing setup.

Cu-K$_\alpha$ radiation of wavelength 1.5404 Å and the diffractogram run with two theta (2θ) range from 10° to 80°. The XRD data were refined by using full proof software. The Rietveld refined XRD pattern peaks confirm the polycrystalline

spinel cubic structure. Scanning electron microscopy (SEM) and energy-dispersive X-ray spectroscopy (EDS) were carried out by using JEOL (Model JSM-840) instrument respectively to understand structural morphology and elemental analysis. The mean grain size of the particles was estimated from SEM micrographs by using ImageJ software. From SEM and EDS to understand structural morphology and elemental analysis. The AC eclectic parameters were measured over a range of frequencies from 50 Hz to 10 MHz using Wayne Kerr 6500B series impedance analyzer. For humidity sensing AC conduction studies, powder samples were pressed in the form of pellet under the hydraulic pressure of 5 tons. Further, two faces of these pellets were painted with silver paste for electrical contact. The pellet was held between two probes and then placed in a glass chamber through a rubber cork and the other end of the electrodes connected to the programmable HIOKI Digital Multimeter to record the resistance corresponding to various RH relative humidities from 11% RH to 97%. The schematic illustration of humidity sensing setup is shown in **Figure 2**.

3. Results and discussion

3.1 XRD analysis

Figure 3 shows the Rietveld refined XRD patterns of as-synthesized $CuFe_{(2-x)}Eu_xO_4$ (where x = 0.00, 0.01, 0.02, 0.03) nanoparticles. XRD patterns of all samples show the polycrystalline spinel cubic structure with space group Fd3m with a small amount of CuO impurity phase. The indexed XRD peaks are well

Figure 3.
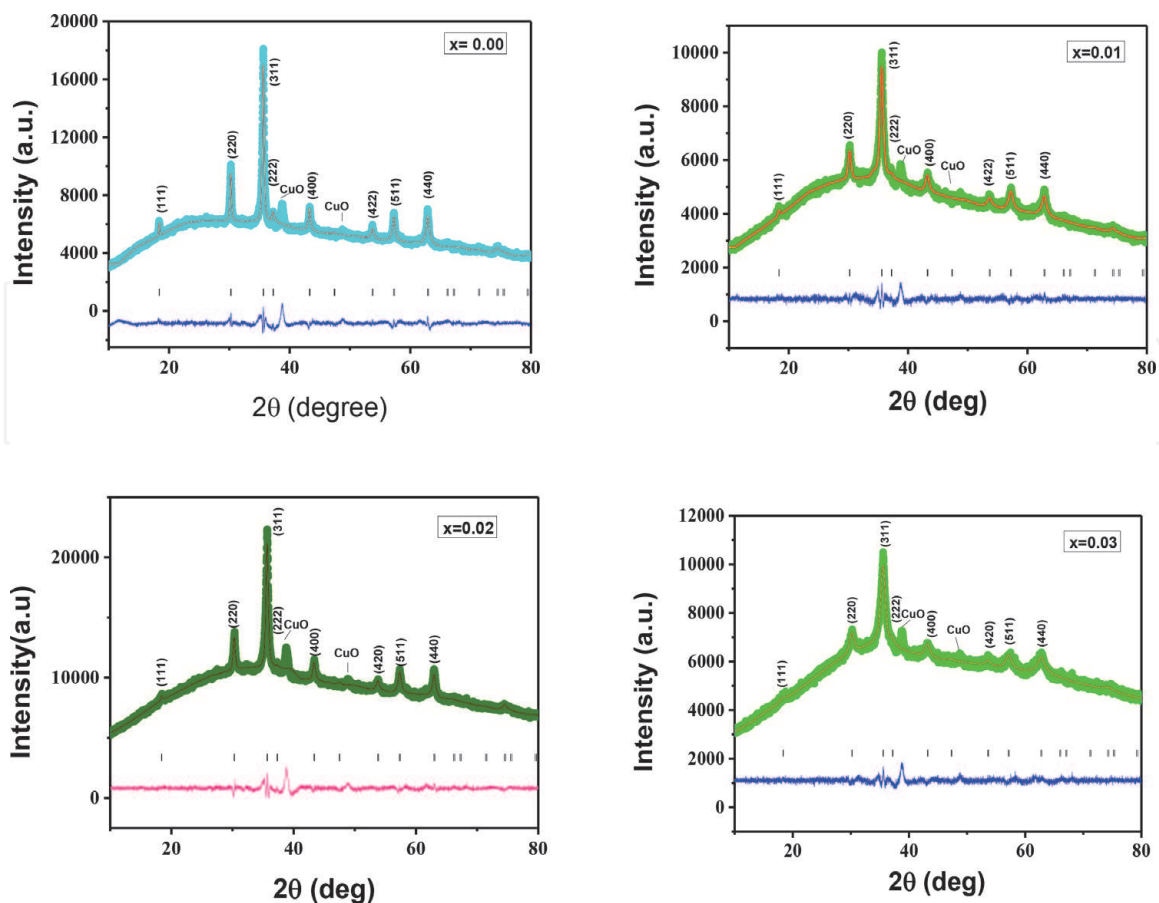*Rietveld refined XRD patterns of the $CuFe_{(2-x)}Eu_xO_4$ (where x = 0.00, 0.01, 0.02, 0.03) nanoparticles.*

matched with spinel cubic structure of JCPDS card number 74-2400 and the CuO impurity peaks observed at 38.87° and 48.96° (JCPDS 80-1268) [7, 8]. The lattice parameter is found to increase with increase in Eu^{3+} concentration due to difference in ionic radius. The ionic radii of Fe^{3+} (0.67 Å) are lesser than that of Eu^{3+} (0.99 Å) ions; this confirms the occupancy of europium on an octahedral site. The average crystallite size of $CuFe_{2-x}Eu_xO_4$ (where x = 0.00, 0.01, 0.02, 0.03) nanoparticles estimated from the Debye-Scherrer relation and the average particle size of all the samples were found to be in the range of 16–51 nm [9]. The strain values are calculated by using equation $\varepsilon = \beta cos\theta / 4$ and are tabulated in **Table 1**. Further, the hopping length of L_A and L_B is calculated, the hopping length increasing with increase in Eu^{3+} concentration. This happened because Fe^{3+} ions are replaced by the relative number of Eu^{3+} in octahedral site and the variation of hopping length of tetrahedral site (L_A) and octahedral site (L_B) is shown in **Table 1**.

3.2 SEM and EDS

The surface morphology and elemental analysis of the $CuFe_{(2-x)}Eu_xO_4$ (where x = 0.00, 0.01, 0.02, 0.03) nanoparticles were performed with scanning electron microscope and energy-dispersive X-ray spectroscope. From **Figure 4(left)** we can clearly see that all the particles are spherical in shape and exhibit smooth surface with an average grain size of 20–40 nm. All samples of the SEM micrographs show highly porous nature, and the appearance of the dry foamy powder is due to the evolution of the gases during the combustion process [10]. **Figure 4(right)** shows the EDS spectrum of $CuFe_{(2-x)}Eu_xO_4$ (where x = 0.00, 0.01, 0.02, 0.03) nanoparticles. The $CuFe_{(2-x)}Eu_xO_4$ (where x = 0.01, 0.02, 0.03) of EDS spectrum depicts Cu, Fe, Eu, and O peaks are clearly seen with Cuo impurity peaks (**Figure 4(right)**). $CuFe_{(2-x)}Eu_xO_4$ (where x = 0.00) of EDS spectrum depicts Cu, Fe, and O peaks are clearly seen with Cuo impurity peak. The Eu^{3+} peak appeared in all samples except when x = 0, and its intensity of Eu^{3+} peak increase with europium concentration increases. The grain size distribution histogram of $CuFe_{(2-x)}Eu_xO_4$ (where x = 0.00, 0.01, 0.02, 0.03) nanoparticles is shown in **Figure 4(left)**, and the average grain size of $CuFe_{(2-x)}Eu_xO_4$ (where x = 0.00, 0.01, 0.02, 0.03) nanoparticles is estimated from SEM micrographs using ImageJ software. The average grain sizes of all the particles are well matched with the crystallite size as shown in **Table 1**.

3.3 Dielectric studies

3.3.1 Variation of frequency with AC conductivity

Figure 5 shows the variation of frequency with AC conductivity plots, respectively, for $CuFe_{(2-x)}Eu_xO_4$ (where x = 0.00, 0.01, 0.02, 0.03) nanoparticles

Eu^{3+} content	Lattice parameters (Å)	Crystallite size D in nm	Volume (Å³)	Strain ϵ (radian)	Space group	Average grain size	Hopping length (Å)	
							L_A	L_B
x = 0.0	8.126	25	539.29	1.38×10^{-3}	Fd3m	28	3.518	2.873
x = 0.01	8.131	16	540.23	2.14×10^{-3}	Fd3m	30	3.520	2.874
x = 0.02	8.143	21	542.71	1.63×10^{-3}	Fd3m	40	3.526	2.879
x = 0.03	8.154	51	544.91	6.98×10^{-3}	Fd3m	33	3.531	2.883

Table 1.
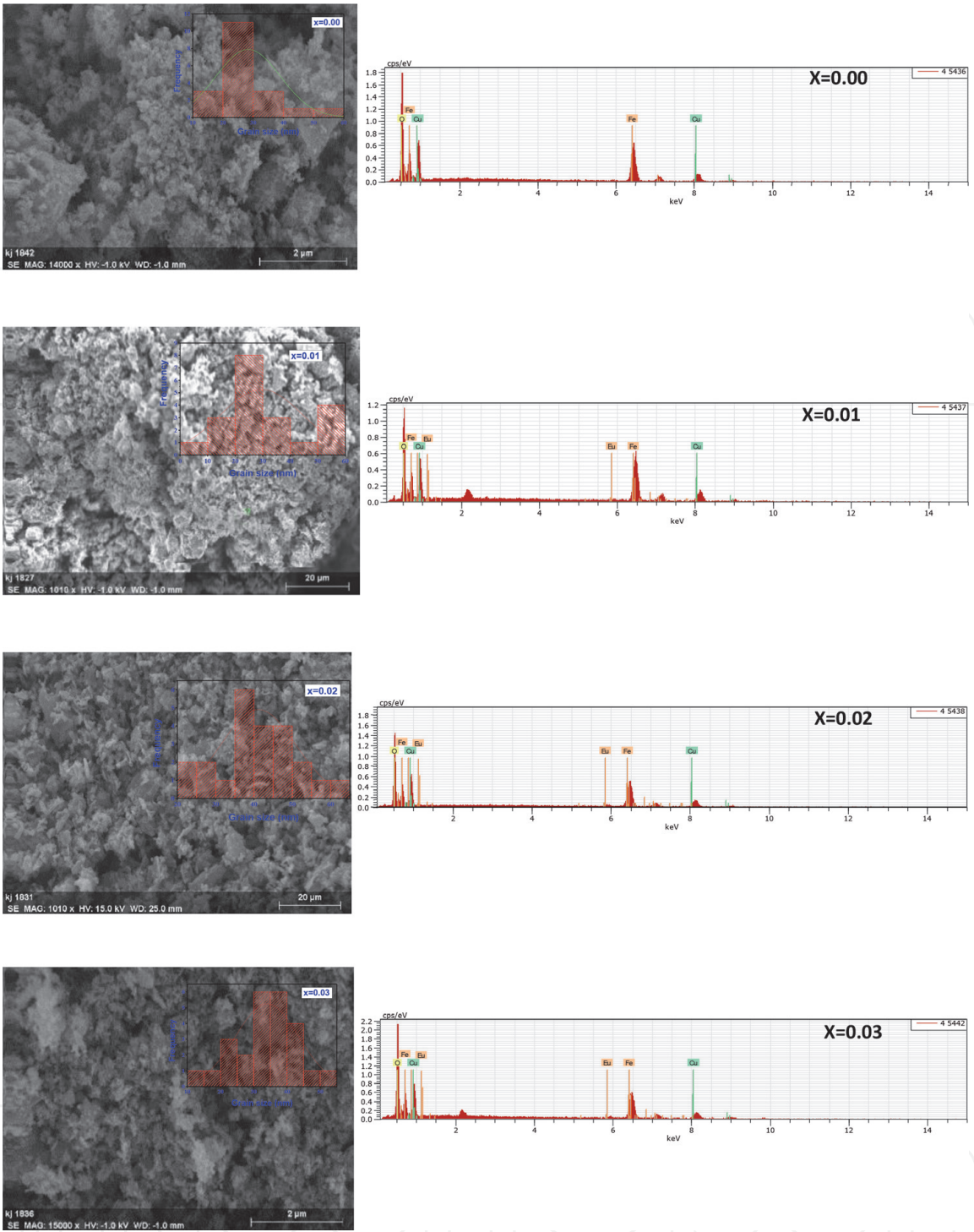*Structural parameters of the CuFe$_{(2-x)}$Eu$_x$O$_4$ (where x = 0.00, 0.01, 0.02, and 0.03) nanoparticles.*

Figure 4.
(Left) SEM micrographs and (right) EDS spectra of the CuFe$_{(2-x)}$Eu$_x$O$_4$ (where x = 0.00, 0.01, 0.02, and 0.03) nanoparticles.

measured over the frequency range of 0.1 kHz to 1 MHz at room temperature. The figure clearly reveals the AC conductivity of each sample increases linearly with frequency. The exchange of electrons between A site and B site enhances the AC conductivity. The sample with a higher concentration of europium ions shows high values of AC conductivity. The substitution of europium ions on the copper ferrites obstructs the exchange of electrons between A sites and B sites, resulting in the decrease in the AC conductivity. At the lower-frequency region, the effect of grains and grain boundary is dominant, and it causes decreases in the exchange of electron between Fe^{2+} ions and Fe^{3+} ions, so small AC conductivity values have been observed. The polarization of all the samples of spinel copper ferrites is increased at high
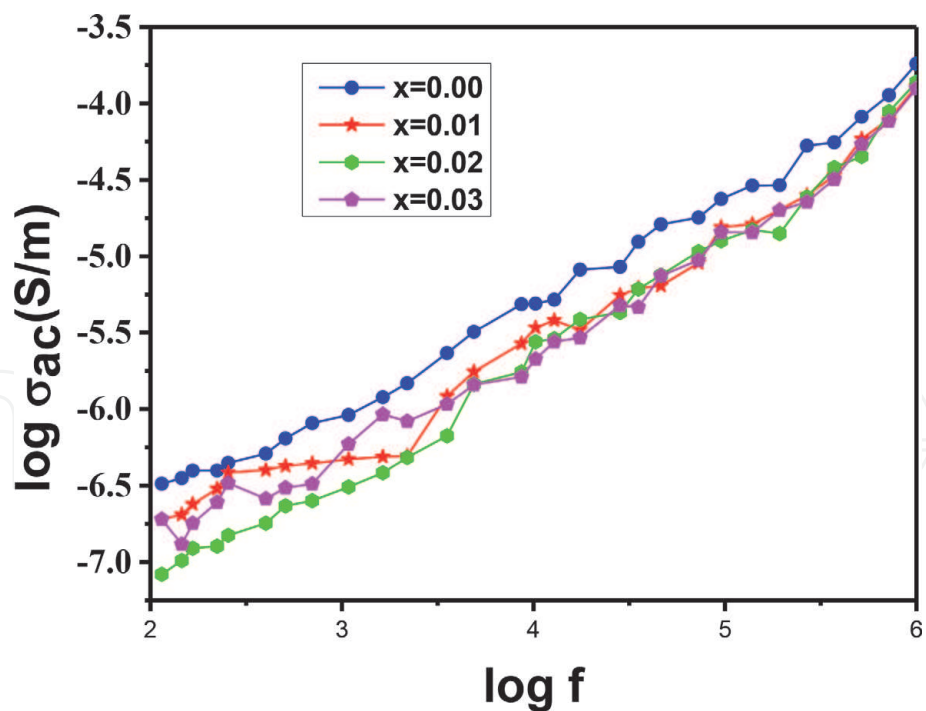
Figure 5.
The variation of frequency with AC conductivity for the $CuFe_{(2-x)}Eu_xO_4$ (where x = 0.00, 0.01, 0.02, and 0.03) nanoparticles.

frequency. In the copper ferrite, the part of the grains is very essential at greater frequency than grain boundary's part; it causes the conduction to be enhanced in spinel ferrites [11]. The doping of europium ions to the Fe^{3+} ions from the octahedral site disrupts the conduction mechanism, and the AC conductivity decreases. The maximum value of AC conductivity is found to be x = 0.00 concentration.

3.3.2 Variation of frequency with real and imaginary part of electric modulus

Figure 6 shows the variation of frequency with real and imaginary parts of electric modulus plots respectively for $CuFe_{(2-x)}Eu_xO_4$ (where x = 0.00, 0.01, 0.02, 0.03) nanoparticles. These were studied over the frequency range of 0.1 kHz to 1 MHz at room temperature. To study the character of grain boundary and grains over the frequency range of 0.1 kHz to 1 MHZ, electric modulus analysis was taken out. For this basis, the graphs plot between real and imaginary parts of electric
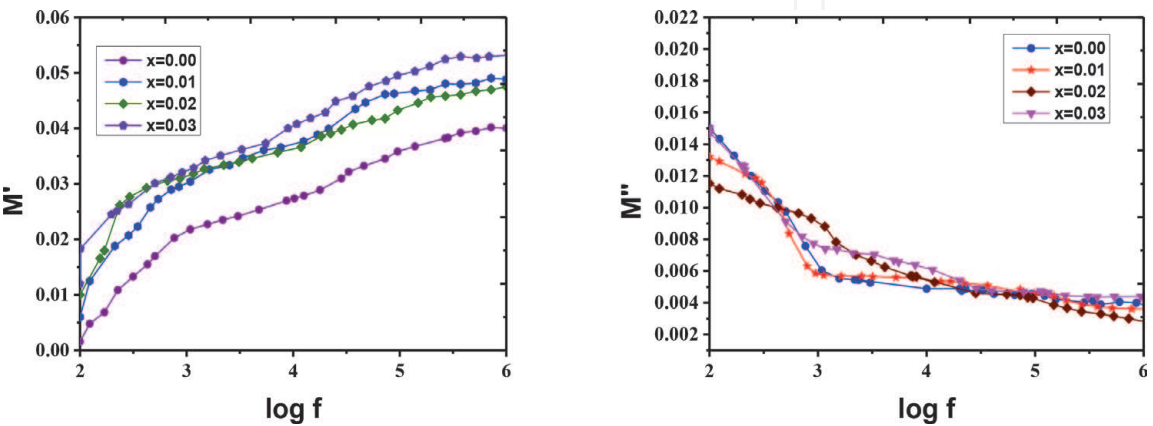

Figure 6.
The variation of frequency with real and imaginary parts of electric modulus for the $CuFe_{(2-x)}Eu_xO_4$ (where x = 0.00, 0.01, 0.02, and 0.03) nanoparticles.

modulus along the y-axis and the frequency along the x-axis were taken. In copper ferrites, the real parts of the electric modulus M' show very low M' values at lower-frequency region and increase linearly with the increase in the frequency of the external applied field [12]. In the case of the imaginary part of electric modulus (M''), high electric modulus at lower-frequency region is shown and again decreases with increase in the frequency of external applied field. The real and imaginary parts of electric modulus were maximum at x = 0.00 concentration.

3.3.3 Cole-Cole plots

Figure 7 shows the imaginary part of electric modulus with real part of electric modulus plots, respectively, for $CuFe_{(2-x)}Eu_xO_4$ (where x = 0.00, 0.01, 0.02, 0.03) nanoparticles at room temperature. To examine the effect of grain boundaries and grains within spinel ferrites, a plot can be drawn between real and imaginary parts of dielectric constant and dielectric loss or using the values of the real and imaginary parts of impedance, but no satisfactory results were obtained from the aforesaid formalisms. The figure plot between real and imaginary parts of dielectric modulus clearly shows the semicircles within the given range of these quantities. The Cole-Cole plots between the real part of the electric modulus and imaginary parts of the electric modulus can give good results. The role of grains and grain boundaries is very good because semicircles are observed at all the samples [9, 12]. The maximum peak of the diameter observed semicircle increases with the substitution of europium rare earth ions. The maximum intensity of peak is observed at x = 0.03 concentration.

Figure 7 shows Cole-Cole (the imaginary part of impedance with real part impedance) plots for $CuFe_{(2-x)}Eu_xO_4$ (where x = 0.00, 0.01, 0.02, 0.03) nanoparticles at room temperature.

In these impedance analysis plots, we observed only one semicircle clearly at x = 0.00 concentration, this study indicating the role of grain boundaries predominated, and the contribution from the grain was not resolved from this impedance analysis [13]. Sivakumar et al. reported a similar result from nanocrystalline cobalt ferrites [14]. The radii of the semicircles decreased with increasing concentration; this sign indicates a decrease in relaxation.

3.4 Humidity sensing studies

3.4.1 Variation of resistance and sensing response with relative humidity

In **Figure 8**, the curves are plotted between the relative humidity along the x-axis and resistance along the y-axis for $CuFe_{(2-x)}Eu_xO_4$ (where x = 0.00, 0.01, 0.02, 0.03) nanoparticles at room temperature. For all samples, the resistances are
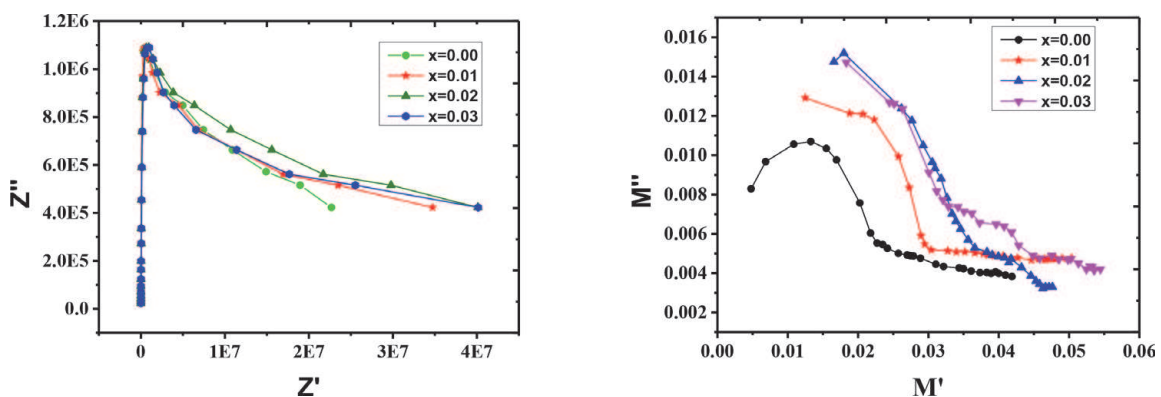

Figure 7.
Imaginary part of electric modulus with real part of electric modulus and the imaginary part of impedance with real part impedance, respectively, for $CuFe_{(2-x)}Eu_xO_4$ (where x = 0.00, 0.01, 0.02, and 0.03) nanoparticles.
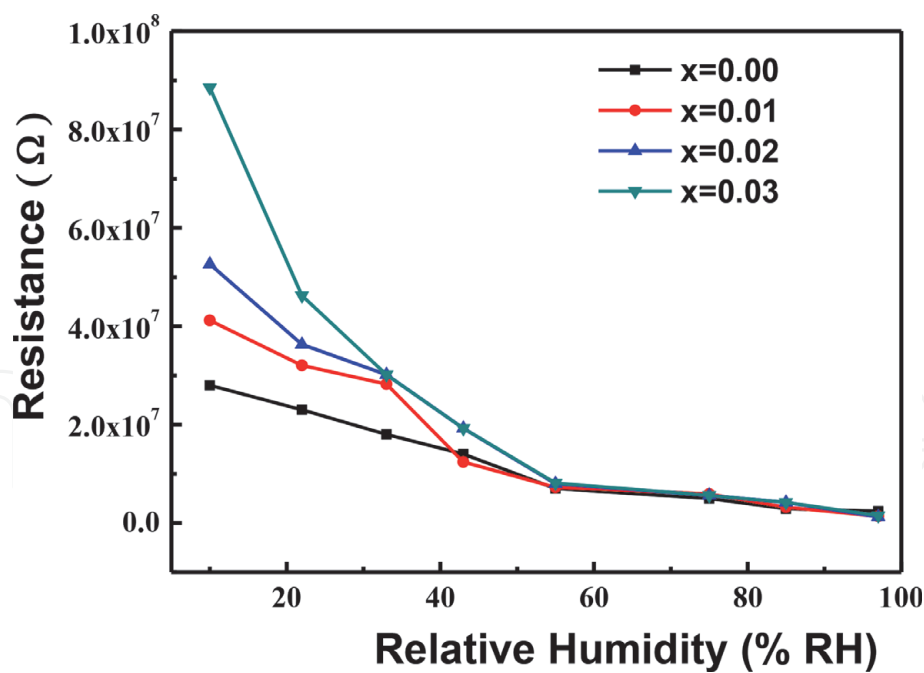
Figure 8.
The variation of resistance with relative humidity for CuFe$_{(2-x)}$Eu$_x$O$_4$ (where x = 0.00, 0.01, 0.02, and 0.03) nanoparticles.

decreased from 1×10^7 Ω to 100×10^7 Ω for relative humidity varying from 11 to 97% RH. From the figure, the maximum variation in resistance is observed for CuFe$_{(2-x)}$Eu$_x$O$_4$ (where x = 0.03) sample as compared to other samples. So, the humidity sensing response of each sample was calculated by using the following equation and plotted against %RH shown in **Figure 9**.

Humidity sensing response

$$= \frac{\text{resistance of lower relative humidity} - \text{resistance at any relative humidity}}{\text{resistance of lower relative humidity.}} \quad (1)$$
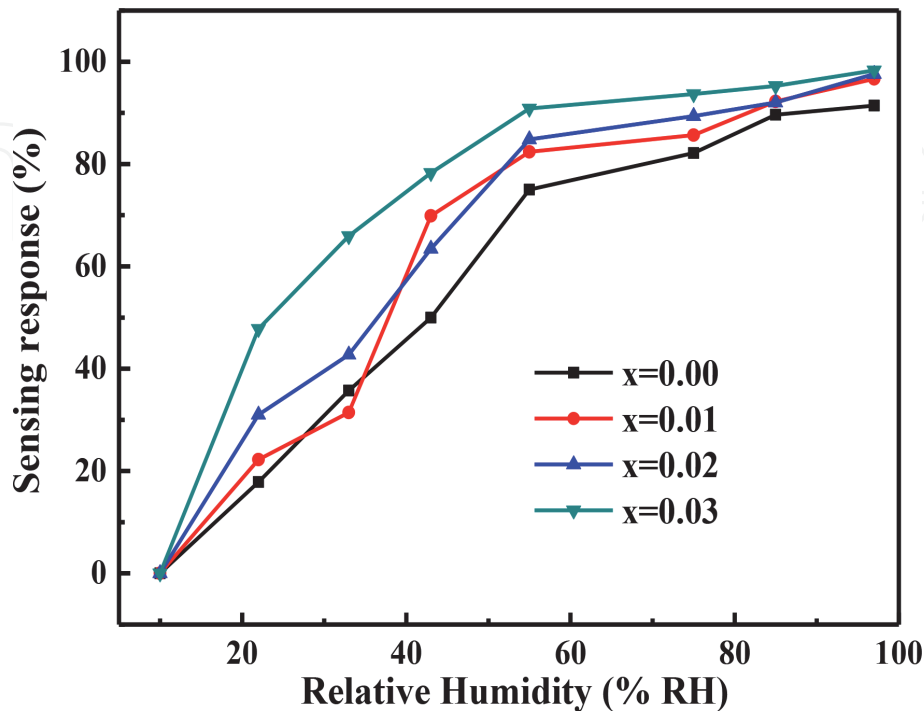

Figure 9.
The variation of sensing response (%) with relative humidity for CuFe$_{(2-x)}$Eu$_x$O$_4$ (where x = 0.00, 0.01, 0.02, and 0.03) nanoparticles.

9

The $CuFe_{(2-x)}Eu_xO_4$ (where x = 0.03) has shown the maximum sensing response; hence it is essential to know its sensing mechanism. The sensing mechanism is discussed on the basis of three sequential steps: chemisorptions, first step of physisorption, and second step of physisorption, followed by capillary condensation. In the initial stage, the water molecule adsorbed to the sensing surface and gets self-ionized to form H^+ and OH^- ions [15].

$$H_2O \Leftrightarrow H^+ + OH^- \tag{2}$$

In the beginning stage, the dissociated OH^- ions get attached to the sensing surface forming a chemisorption layer, and H^+ ions are released. These chemisorbed two OH^- ions form a hydrogen bond with the neighboring water molecule to form bulk water (H_3O^+). This forms the first physisorbed layer. Thus formed bulk water dissociates to form H_2O and H^+ ion. The released H^+ ions transfer from one water molecule to another through the braking and making of bonds. This is in accordance with the Grotthuss mechanism [16].

$$2H_2O \rightarrow H_3O^+ + OH^- \tag{3}$$

$$H_3O^+ \rightarrow H_2O + H^+ \tag{4}$$

As the RH increases, the physisorbed water molecules get piled up on one another forming the second step of physisorption. At the last stage, the adsorbed water molecule condenses in the capillary pores, leading to increase in the protonation. These results in the decrease in the resistance and in turn increase in its conductivity.

3.4.2 Sensing response and recovery

Nowadays, the sensing response and recovery time characteristics and stability testing are required for device fabrication of humidity sensing material. The response and recovery time were measured only for $CuFe_{(2-x)}Eu_xO_4$ (where x = 0.03) because of good sensing response as compared to other samples. In response and recovery time studies, we used two chambers, in that one chamber containing lower relative humidity of 11% RH another of higher relative humidity of 95% RH. The sensing response time of 63 s was recorded when the sample was moved from relative humidity of 11% RH to relative humidity of 97% RH, and the recovery time of 164 s was recorded when sample was moved from relative humidity of 97% RH to relative humidity of 11% RH (**Figure 10**). The difference between sensing response time and recovery time is small. These studies clearly show that the response and recovery time of Eu^{3+}-doped $CuFe_2O_4$ sample is slightly better than response and recovery time of nickel copper-zinc ferrite synthesized by coprecipitation method [17].

3.4.3 Stability

Stability testing is one of the important tests for practical application in device fabrication of sensing material. For stability testing, $CuFe_{(2-x)}Eu_xO_4$ (where x = 0.03) sample pellet was tested at relative humidity of 97% RH and 55% RH for every 10 days in 2 months. **Figure 11** shows the stability curves at 55% RH and 97% RH for $CuFe_{(2-x)}Eu_xO_4$ (where x = 0.03) sample at room temperature. The figure clearly indicates that both relative humidity samples show highly stable response at room temperature during that period. So, sample shows that humidity sensing material is highly stable at larger concentration of europium-doped copper ferrite at
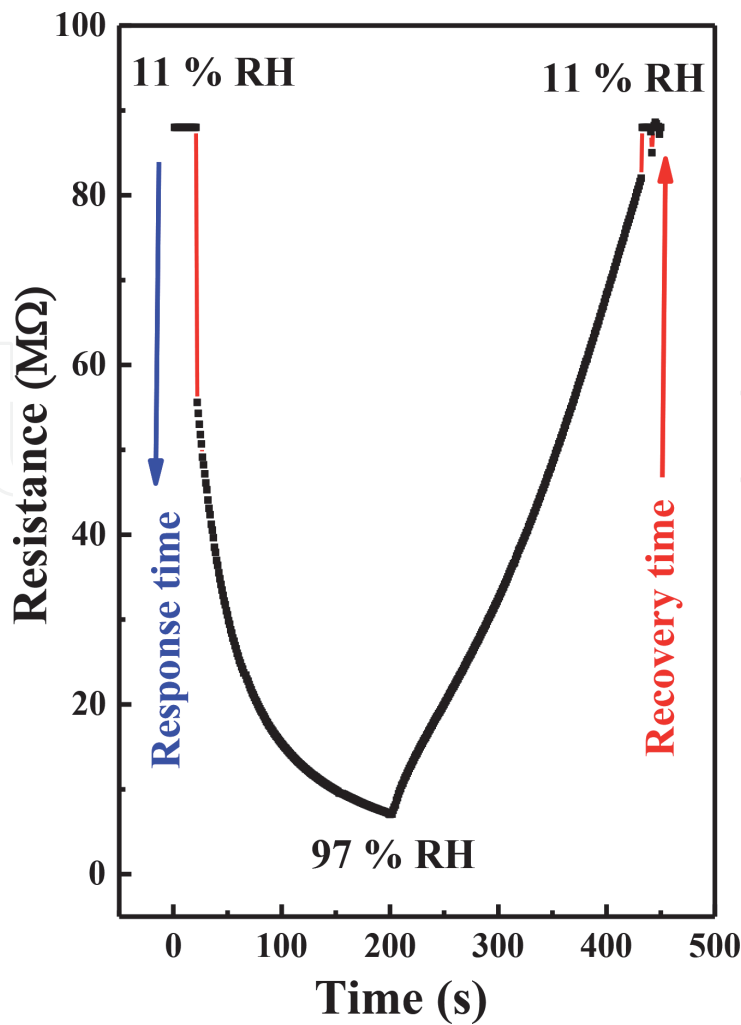
Figure 10.
The sensing response and recovery characteristic for CuFe$_{(2-x)}$Eu$_x$O$_4$ (where x = 0.00, 0.01, 0.02, and 0.03) nanoparticles.

Figure 11.
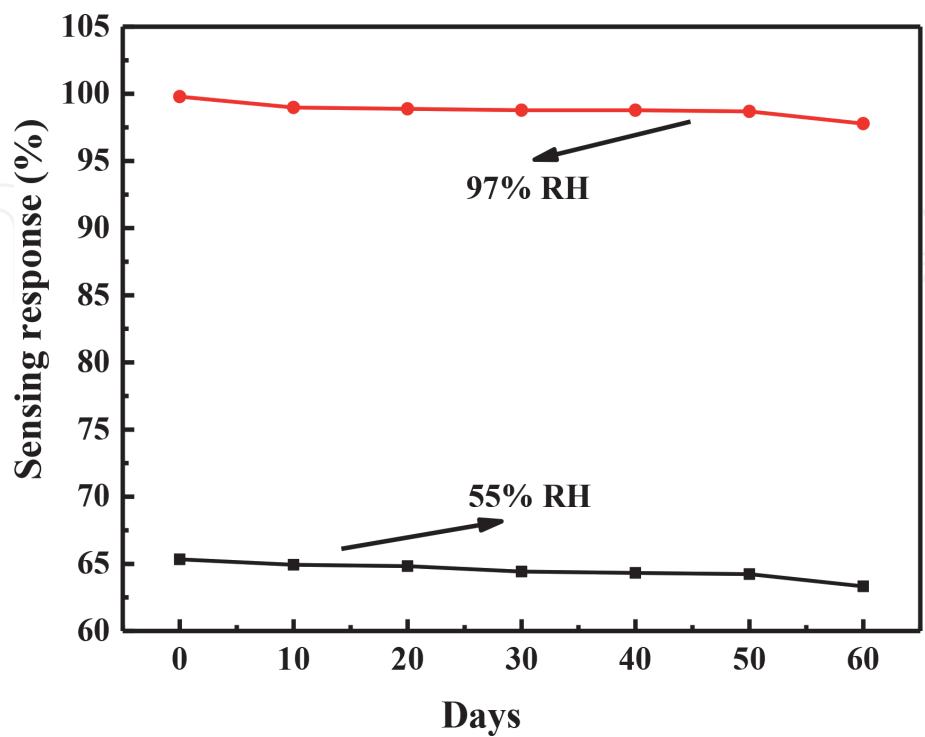*The humidity sensing stability characteristic for CuFe$_{(2-x)}$Eu$_x$O$_4$ (where x = 0.00, 0.01, 0.02, and 0.03) nanoparticles.*

room temperature and this is the proof for good practical application. The less concentration of europium-doped copper ferrite sample was not tested for stability because at lower concentration samples show less sensing response compared to higher concentration. However low sensing response ferrites also have good potential applications such as electronic and battery applications [17, 18].

4. Conclusions

The $CuFe_{(2-x)}Eu_xO_4$ (where x = 0.00, 0.01, 0.02, 0.03) nanoparticles were synthesized by solution combustion method using mixture of fuels for the first time. XRD patterns reveal the polycrystalline spinel cubic structure having space group Fd3m with small amount of impurity phases at 38.87° and 48.96°. The SEM micrograph reveals the formation of dry foamy powders during combustion process and porous nature of the sample. The average grain size of the samples was measured from SEM micrographs. The chemical composition was analyzed by using EDS analysis. The dielectric parameters vary with frequency. In the copper ferrite, the role of the grains is very essential at greater frequency as compared to grain boundary's role. The radii of the semicircles decreased with increasing concentration; this sign indicates a decrease in relaxation. The humidity sensing response at higher concentration is very good as compared to other concentration. The response and recovery curve time was good as compared to other ferrite samples. The sample shows high stability at higher concentration with good sensing response for sensor applications. At lower concentration, europium-doped sample shows low sensing response; however, the low sensing responsible ferrites are used in battery and electronic applications.

Author details

I.C. Sathisha[1], K. Manjunatha[1], V. Jagadeesha Angadi[2*], B. Chethan[3],
Y.T. Ravikiran[4], Vinayaka K. Pattar[5], S.O. Manjunatha[6]
and Shidaling Matteppanavar[7]

1 Department of Physics, School of Engineering, Presidency University, Bangalore,
India

2 Department of Physics, P.C. Jabin Science College, Hubballi, India

3 Department of Physics, Research Centre, JNN College of Engineering, Shimoga,
India

4 Department of PG Studies and Research in Physics, Government Science College,
Chitradurga, India

5 New Chemistry Unit, Jawaharlal Nehru Centre for Advanced Scientific Research,
Bangalore, India

6 Department of Physics, M.S. Ramaiah University of Applied Sciences, Bengaluru,
India

7 Department of Physics, Basavaprabhu Kore Arts, Science and Commerce College,
Chikodi, India

*Address all correspondence to: jagadeeshbub@gmail.com

IntechOpen

References

[1] Jansi Rani B, Saravanakumar B, Ravi G, Ganesh V, Ravichandran S, Yuvakkumar R. Optical and magnetic properties of $CuFe_2O_4$ nanoparticles. Journal of Material Science: Materials in Electronics. 2018;**29**:1975-1984

[2] Srinivasamurthy KM, Angadi VJ, Kubrin SP, Matteppanavar S, Kumar PM, Rudraswamy B. Evidence of enhanced ferromagnetic nature and hyperfine interaction studies of Ce-Sm doped Co-Ni ferrite nanoparticles for microphone applications. Ceramics International. 2018;**44**:18878-18885

[3] Naik CC, Salker AV. Investigation of the effect of fractional In^{3+} ion substitution on the structural, magnetic, and dielectric properties of Co-Cu ferrite. Journal of Physics and Chemistry of Solids. 2019;**133**:151-162

[4] Kurian J, Mathew MJ. Structural, optical and magnetic studies of $CuFe_2O_4$, $MgFe_2O_4$ and $ZnFe_2O_4$ nanoparticles prepared by hydrothermal/solvothermal method. Journal of Magnetism and Magnetic Materials. 2017;**451**:121-130

[5] Manjunatha K, Sathish IC, Kubrin SP, Kozakov AT, Lastovina TA, Nikolskii AV, et al. X-ray photoelectron spectroscopy and low temperature Mössbauer study of Ce^{3+} substituted $MnFe_2O_4$. Journal of Materials Science: Materials in Electronics. 2019;**30**: 10162-10171

[6] Jagadeesha Angadi V, Matteppanavar S, Katti RB, Rudraswamy B, Praveena K. Breaking of ferrimagnetic ordering in Sc^{3+} doped Mn-Zn ferrites due to high energy Gamma irradiation. AIP Conference Proceedings. 2017;**1832**: 130040

[7] Jagadeesha Angadi V, Rudraswamy B, Sadhana K, Ramana Murthy S, Praveen K. Effect of $Sm^{3+}-Gd^{3+}$ on structural, electrical and magnetic properties of Mn-Zn ferrites synthesized via combustion route. Journal of Alloys and Compounds. 2016;**656**:5-12

[8] Othman I, Abu Haija M, Ismail I, Zain JH, Banat F. Preparation and catalytic performance of $CuFe_2O_4$ nanoparticles supported on reduced graphene oxide ($CuFe_2O_4$/rGO) for phenol degradation. Materials Chemistry and Physics. 2019;**238**:121931

[9] Srinivasamurthy KM, Manjunatha K, Sitalo EI, Kubrin SP, Sathish IC, Matteppanavar S, et al. Effect of Ce^{3+} substitution on the structural, morphological, dielectric, and impedance spectroscopic studies of Co−Ni ferrites for automotive applications. Indian Journal of Physics. 2018;**1**:1-12

[10] Galivarapu JK, Kumar D, Banerjee A, Sathe V, Aquilanti G, Rath C. Effect of size reduction on cation distribution and magnetic transitions in $CoCr_2O_4$ multiferroic: EXAFS, magnetic and diffused neutron scattering measurements. RSC Advances. 2016;**6**:63809-63819

[11] Sakthisabarimoorthi A, Martin Britto SA, Dhas R, Jose RM. Influence of erbium doping on the electrical behaviour of $CaCu_3Ti_4O_{12}$ ceramics probed by impedance spectroscopy analysis. Materials Research Bulletin. 2018;**106**:81-92

[12] Oumezzine E, Hcini S, Rhouma FIH, Oumezzine M. Frequency and temperature dependence of conductance, impedance and electrical modulus studies of $Ni_{0.6}Cu_{0.4}Fe_2O_4$ spinel ferrite. Journal of Alloys and Compounds. 2017;**726**:187-194

[13] Sivakumar N, Narayanasamy A, Shinoda K, Chinnasamy CN, Jeyadevan B, et al. Electrical and

magnetic properties of chemically
derived nanocrystalline cobalt ferrite.
Journal of Applied Physics. 2007;**102**:
013916

[14] Angadi VJ, Choudhury L,
Sadhana K, Liu H-L, Sandhya R,
Matteppanavar S, et al. Structural,
electrical and magnetic properties of
Sc^{3+} doped Mn-Zn ferrite nanoparticles.
Journal of Magnetism and Magnetic
Materials. 2017;**424**:1-11

[15] Chethan B, Raj Prakash HG,
Ravikiran YT, Vijayakumari SC,
Ramana CHVV, Thomas S, et al.
Enhancing humidity sensing
performance of polyaniline/water
soluble graphene oxide composite.
Talanta. 2019;**196**:337-344

[16] Babu Reddy LP, Megha R, Raj
Prakash HG, Ravikiran YT,
Ramana CHVV, Vijaya Kumari SC, et al.
Copper ferrite-yttrium oxide (CFYO)
nanocomposite as remarkable humidity
sensor. Inorganic Chemistry
Communications. 2019;**99**:180-188

[17] Jeseentharani V, George M,
Jeyaraj B, Dayalan A, Nagaraja KS.
Synthesis of metal ferrite (MFe_2O_4,
M = Co, Cu, Mg, Ni, Zn) nanoparticles
as humidity sensor materials. Journal of
Experimental Nanoscience. 2012;**8**:1-13

[18] Chethan B, Raj Prakash HG,
Ravikiran YT, Vijayakumari SC,
Thomas S. Polypyyrole based core-shell
structured composite based humidity
Sensor operable at room temperature.
Sensors & Actuators: B. Chemical. 2019;
296:126639